SOILS AND FOUNDATIONS Vol. 47, No. 5, 919–929, Oct. 2007
Japanese Geotechnical Society

AN ELASTOPLASTIC MODEL FOR UNSATURATED ROCKFILLS AND ITS SIMULATIONS OF LABORATORY TESTS

YUJI KOHGO[i], ISAMU ASANO[ii] and YOICHI HAYASHIDA[iii]

ABSTRACT

This paper describes an elastoplastic model for rockfills and simulations of laboratory test by using the model. Rockfills express remarkable shear strength reductions and compressive deformations due to saturation. The authors have already developed elastoplastic models to represent the mechanical properties of unsaturated soils. Two suction effects were taken into account in the models. However for rockfills, one suction effect: an increase in suction enhances yield stresses and affects resistance to plastic deformations, remarkably appears. The effect may be evaluated by formulating state surfaces. In this paper, a model proposed by authors is modified for rockfills. To verify the elastoplastic model for rockfills, simulations of oedometer and triaxial compression tests were carried out. The simulation results could well express the volume change and shear behavior of the rockfill, especially the influence of water contents.

Key words: (collapsed settlement), constitutive equation, numerical analysis, rockfill, suction, unsaturated soil (**IGC**: D4/D5/D6/E12)

INTRODUCTION

In order to solve cost reductions and environmental issues in constructions and rehabilitations of dams, it is very important to use low quality rockfills (kohgo et al., 2007) as construction materials. A main problem for use of low quality ones as the construction materials seems to be that the differences between saturated and unsaturated mechanical behavior are sometimes greater than those in high quality ones.

The mechanical properties of rockfills are closely related to breakage properties of rock particles (Marsal, 1972; Marachi et al., 1968). The breakage properties are sometimes strongly affected by the degree of saturation (Terzaghi, 1960; Kohgo et al., 2007). Especially, compression deformations due to saturation, called saturation collapse, seems to be induced by the difference between saturated and unsaturated breakage properties of rock particles. The saturation collapse causes cracks on crests of dams and it may become one of the causes of hydraulic fracturing. Nobari and Duncan (1972) proposed a procedure for calculation of collapse deformations in which unbalanced forces were calculated from the differences between stress-strain relationships of saturated and unsaturated specimens and the collapse deformations were estimated by the unbalanced forces. They adopted a nonlinear elastic model: Duncan-Chang model to describe the stress-strain relationships. As the saturation collapse is the phenomenon that arises from the breakage of rock particles, most of the deformations should be regarded as plastic deformations. Oldecop and Alonso (2001) proposed an elastoplastic model that was only valid to express compression properties of unsaturated rockfills. Thus elastoplastic models, which can describe the saturated and unsaturated mechanical behavior (both compression and shear) of rockfills, have not been proposed.

The purpose of this paper is to present an elastoplastic model for rockfills and simulations of laboratory tests by using the model. The model should have potentials to describe the saturated and unsaturated mechanical behavior of rockfills including from low to high quality rockfills. Using the consolidation analysis method proposed by Kohgo (1995, 1997) combined with this elastoplastic model, we might not only check the performance of the dams constructed by low quality rockfills but also design effective zonings. Our original elastoplastic model (Kohgo et al., 1993b) will be modified to express mechanical behavior of saturated and unsaturated rockfills. In order to verify the elastoplastic model, simulations of oedometer and triaxial compression tests are conducted.

AN ELASTOPLASTIC MODEL FOR ROCKFILL MATERIALS

We only consider the time-independent mechanical properties, here.

[i] Associated Professor, Tokyo University of Agricultural and Technology, Japan (kohgo@ce.tuat.ac.jp).
[ii] Research Staff, Agriculture Forestry and Fishers Research Council, Japan.
[iii] Researcher, Department of Geotechnical and Hydraulic Engineering, National Institute for Rural Engineering, Japan.
The manuscript for this paper was received for review on December 8, 2006; approved on May 29, 2007.
Written discussions on this paper should be submitted before May 1, 2008 to the Japanese Geotechnical Society, 4-38-2, Sengoku, Bunkyo-ku, Tokyo 112-0011, Japan. Upon request the closing date may be extended one month.

At first, stress notations used in this paper are defined as follows:

$$s = u_a - u_w, \tag{1}$$

$$s^* = \langle s - s_e \rangle, \tag{2}$$

$$p' = \frac{1}{3}(\sigma_1' + \sigma_2' + \sigma_3'), \tag{3}$$

$$q = \sigma_1' - \sigma_3', \tag{4}$$

where s is suction or matric suction, u_a is pore air pressure, u_w is pore water pressure, s^* is effective suction, s_e is air entry suction, σ_1', σ_2', σ_3' are three effective principal stresses, p' is mean effective stress, q is deviator stress and the brackets $\langle\ \rangle$ denote the operation $\langle z \rangle = 0$ at $z < 0$ and $\langle z \rangle = z$ at $z \geq 0$.

Suction Effects

It is necessary to consider two suction effects to represent exactly the mechanical properties of unsaturated soils (Kohgo et al., 1993a). The two suction effects are as follows:

(1) An increase in suction increases effective stresses,
(2) An increase in suction enhances yield stresses and affects the resistance to plastic deformations.

The first suction effect controls changes of the shear strength on the wet side of the critical state (normally consolidation or lightly overconsolidated sides) due to suction, volume reductions due to an increase in suction (drying) and swellings due to a decrease in suction (wetting). The suction effect may be evaluated by using the relationship between suction and shear strength values at the critical state (Kohgo et al., 1993a).

The second suction effect controls both changes of the shear strength on the dry side of the critical state (heavily overconsolidated side) due to suction and volume reductions due to a decrease in suction, namely saturation collapse. The suction effect can be estimated by formulating the state surface. Because state surfaces express elastoplastic volume changes of unsaturated soils (Kohgo, 1987) and the effect can be evaluated by using the state surface concept when plastic volumetric strain is regarded as a hardening parameter (Kohgo et al., 1993a).

It is convenient to consider three partially saturation conditions shown in Fig. 1 in order to understand the suction effects (Kohgo et al., 1993a). The three conditions are insular air, pendular and fuzzy saturation conditions. In the insular air saturation condition, pore air only exits as air bubbles surrounded by water (*see* Fig. 1(a)). From some experimental results (Gan et al., 1988; Fleureau et al., 1993), Terzaghi's effective stress equation is valid in this condition. Then the first suction effect is only effective. It may be namely regarded as the condition where pores are filled with a single compressible fluid mixed with air and water.

In the pendular saturation condition, water is only retained in the menisci formed around grain contact points (*see* Fig. 1(b)). Suction can only induce a force named capillary force. The capillary force acts perpendicularly on grain contact points and attracts soil particles together. Then it is obvious from the friction law that this force restrains relative sliding between soil particles. As most of plastic deformations are due to relative sliding between soil particles, an increase in capillary force inhibits the plastic deformations. The second suction effect is namely effective in this saturation condition.

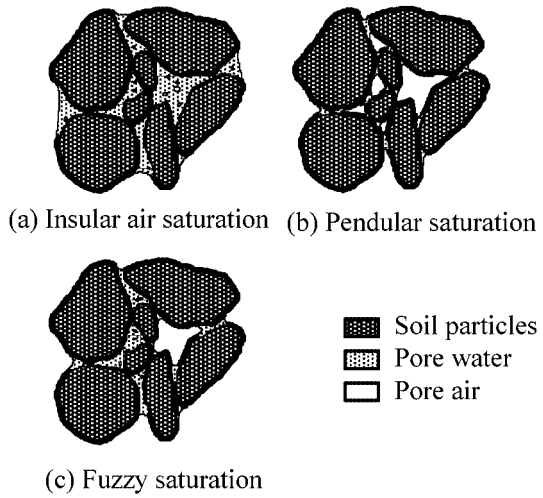

Fig. 1. Possible saturation conditions in real soils

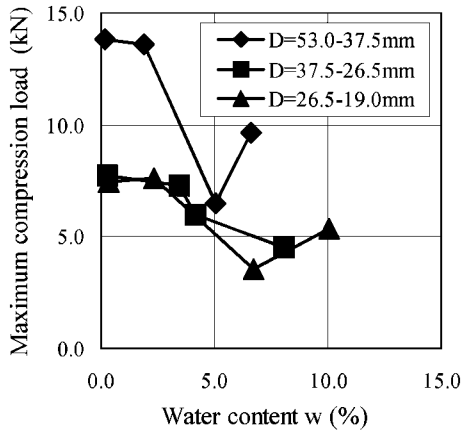

Fig. 2. Relationships between mean maximum compression loads of particles within vertical displacements ≤ 2 mm and water contents for a rockfill named Material S

In rockfills, the mechanism related to the second suction effect is different from that of unsaturated soils. Deformations (exactly plastic deformations) of rockfills may be generally due to breakage of rock particles. An example of relationships between compression loads (breakage strength) and water contents for rock particles can be seen in Fig. 2 (Kohgo et al., 2007). The breakage strength of rock particles may mostly decrease with an increase in water content or a decrease in suction, so more external loads need to be applied to unsaturated rockfill specimens than those to saturated ones to induce the same plastic deformations. As a result, the second suction effect is also valid for rockfills.

In the fuzzy saturation, which is the transitional condition from the insular air to the pendural saturation condi-

tions during drainage, the situation in small pores is similar to that in the insular air saturation condition while the one in large pores is close to that in the pendular saturation condition (*see* Fig. 1(c)). Then, we have to consider two suction effects in this saturation condition.

These three partially saturation conditions can be divided by utilizing a soil-water retention curve shown in Fig. 3. When suction is smaller than the air entry value, the condition is insular air. When suction is very high, the condition is pendular. The fuzzy saturation lies between the insular air and pendular saturation conditions.

In the formulation of elastoplastic models for unsaturated soils, it was necessary to formulate not only effective stress equations but also state surfaces for unsaturated soils. In rockfills, if suction is applied from the full saturation condition, the saturation condition will immediately come into the pendural saturation condition by small application of suction as shown in Fig. 4 where symbols express mean experimental values obtained from the soil column tests (Kohgo et al., 2007). Then, it is sufficient to take only the second suction effect into account when suction is higher than air entry suction. This fact is also seen in Fig. 5. Figure 5 shows typical results of triaxial compression tests for saturated and unsaturated (air dry) specimens (Kohgo et al., 2007). The first suction effect may be evaluated by using the relationship between suction and shear strength values at the critical state (Kohgo et al., 1993a). Then it is not necessary to take account of the first suction effect if both unsaturated and saturated specimens have the same shear strength at the critical state. It is obvious from Fig. 5 that shear strengths of both saturated and unsaturated specimens with the same confining pressures reach almost the same values at the ultimate states that are consistent with their critical state. Suction effects for soils and rockfills are summarized in Table 1.

The effective stress equations for rockfills are as follows:

$$\sigma' = \sigma - u_a + s \quad (s \le s_e), \tag{5}$$

$$\sigma' = \sigma - u_{ae} + s_e \quad (s > s_e), \tag{6}$$

where σ' is effective stress, σ is total stress and u_{ae} is pore air pressure at air entry. Equation (5) is consistent with Terzaghi's effective stress equation, while supposing $u_{ae} = u_{we}$ at air entry, the assumption that Bishop's parameter $\chi = 0$ in Eq. (6) is valid. Where u_{we} is pore water pressure at air entry.

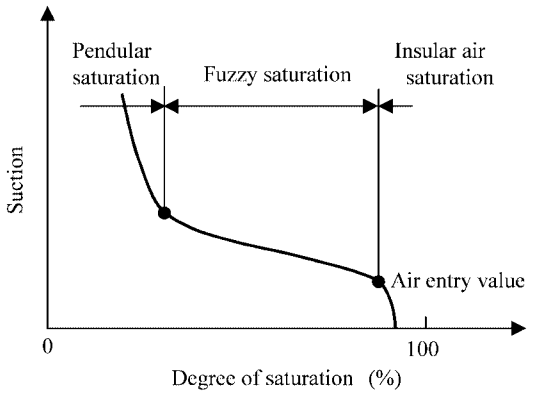

Fig. 3. A typical soil water retention curve

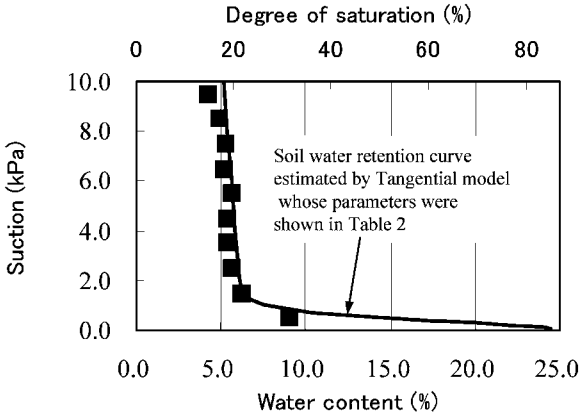

Fig. 4. A typical soil water retention curve for a rockfill named Material S (Symbols: experimental data)

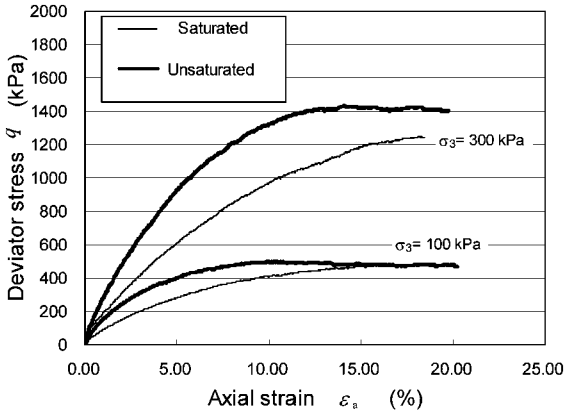

Fig. 5. Comparison between triaxial compression test results of saturated and unsaturated specimens in a rockfill named Material S

Table 1. Suction effects for soils and rockfills

Soil type	Soils			Rockfills		
Saturation condition	Insular air	Fuzzy	Pendural	Insular air	Fuzzy	Pendural
The first suction effect	○	○	×	○	×	×
The second suction effect	×	○	○	×	×	○
Mechanism of the second suction effect	Due to capilary force			Due to breakage of rock particles		

○: Consideration, ×: Nonconsideration

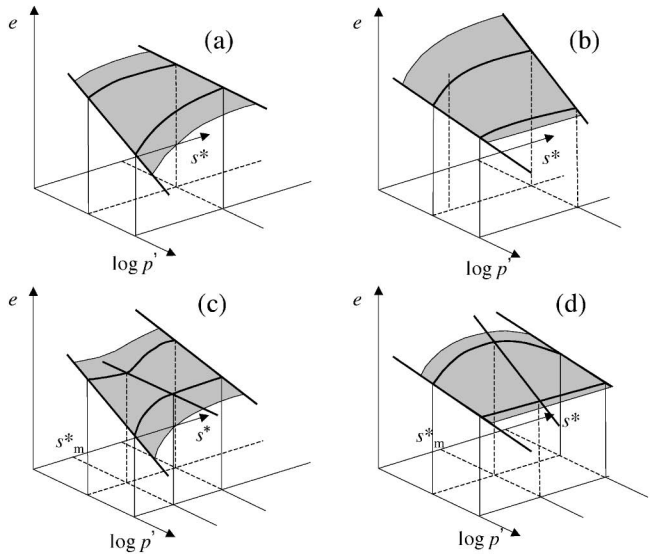

Fig. 6. Various state surfaces for geomaterials

Modeling of State Surface

The second suction effect can be estimated by formulating the state surface. The shape of the state surface depends on the types of soils (Kohgo et al., 2001). The state surfaces can be generally plotted in the space with the axes: effective mean stress p', effective suction s^* and void ratio e. Here four shapes of state surfaces are taken into account. Figure 6 shows the possible shapes of state surfaces. Figure 6(a) shows the state surface where the value of λ^* (slope of e-log p' curves) monotonously decreases as the value of s^* increases, while Fig. 6(b) shows the opposite case where the value of λ^* monotonously increases. Figures 6(c) and (d) show the cases where the state surface has the minimum and maximum slope values, respectively. The state surfaces may be expressed as:

$$e = -\lambda^* \log p' + \Gamma^*, \tag{7}$$

$s^* \le s^*_m$

$$\lambda^* = \lambda + \frac{\lambda^*_{f1} s^*}{s^* + a^*_1}, \tag{8}$$

$$\Gamma^* = e^0_{01} + \frac{(\Gamma - e^0_{01})\lambda^*}{\lambda}, \tag{9}$$

$s^* > s^*_m$

$$\lambda^* = \lambda^*_m + \frac{\lambda^*_{f2}(s^* - s^*_m)}{(s^* - s^*_m) + a^*_2}, \tag{10}$$

$$\Gamma^* = e^0_{02} + \frac{(\Gamma^*_m - e^0_{02})\lambda^*}{\lambda^*_m}, \tag{11}$$

where λ^* is slope of e-log p' curves, Γ^* is void ratio of e-log p' curves at $p' =$ unit, λ and Γ are values of λ^* and Γ^* at saturation, respectively, s^*_m is suction where the state surface has the minimum or maximum slope values, $\lambda^* = \lambda^*_m$ at $s^* = s^*_m$, $\Gamma^* = \Gamma^*_m$ at $s^* = s^*_m$, and e^0_{01}, e^0_{02}, λ^*_{f1}, λ^*_{f2}, a^*_1 and a^*_2 are material parameters.

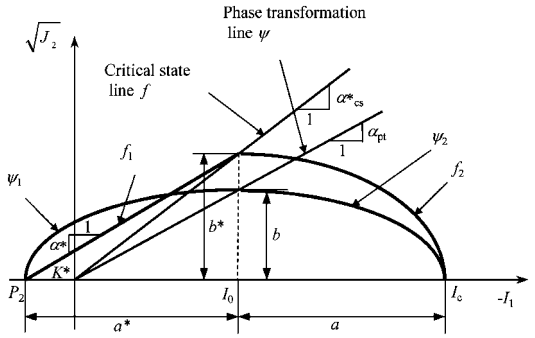

Fig. 7. Normal yield surfaces and plastic potential functions of the elastoplastic model proposed

Generalized Elastoplastic Model for Rockfills

The model described here is modified on the base of Kohgo's model (Kohgo et al., 1993b). The model belongs to cyclic plasticity. In the formulation of the elastoplastic model, compression stresses are assumed to be negative.

As a subloading surface model is used here, we have to define normal yield and loading surfaces. The normal yield surfaces are consistent with the yield surfaces in classic plasticity. This model has two yield surfaces, shown as in Fig. 7. One is the Mohr-Coulomb type failure surface (f_1) and the other is the elliptical cap model with corners (f_2). Both are connected on the critical state line. The yield functions are the same as those defined by Kohgo et al. (1993b).

$$f = f(I_1, J_2, \theta) = \alpha^*_{cs} I_1 + \frac{\sqrt{J_2}}{g(\theta)} = 0, \tag{12}$$

$$f_1 = f_1(I_1, J_2, \theta) = \alpha^* I_1 + \frac{\sqrt{J_2}}{g(\theta)} - K^* = 0, \tag{13}$$

$$f_2 = f_2(I_1, J_2, \theta) = b^{*2}(I_1 - I_0)^2 + a^2 \frac{J_2}{g(\theta)^2} - a^2 b^{*2} = 0, \tag{14}$$

$$g(\theta) = \frac{3 - \sin\phi'}{2(\sqrt{3}\cos\theta - \sin\theta \sin\phi')}, \tag{15}$$

where f is the critical state line, f_1 is the failure surface, f_2 is the cap surface, I_1 is the first stress invariant, J_2 is the second invariant of deviator stress, θ is Lode angle and I_0, a, b^*, K^*, α^* and α^*_{cs} are defined in Fig. 7. Kohgo et al. (1993b) have presented the details.

Following two elliptical plastic potential functions are adopted. They are connected on a phase transformation line as shown in Fig. 7.

$$\psi_1 = b^2(I_1 - I_0)^2 + a^{*2} J_2 - a^{*2} b^2 = 0 \quad (I_0 < I_1 \le P_2), \tag{16}$$

$$\psi_2 = b^2(I_1 - I_0)^2 + a^2 J_2 - a^2 b^2 = 0 \quad (I_c < I_1 \le I_0), \tag{17}$$

where a^* and b are defined as follows.

$$a^* = P_2 - I_0, \tag{18}$$

$$b = -\alpha_{pt} I_0. \tag{19}$$

The slope of α_{pt} is evaluated as follows so that the slope is consistent with the slope of Mohr-Coulomb failure

function (Zienkiewicz and Humpheson, 1977).

$$\alpha_{pt}=\frac{2\sin\phi'_{pt}}{\sqrt{3}\,(3-\sin\phi'_{pt})} \quad \text{at axisymmetric compression,} \tag{20}$$

$$\alpha_{pt}=\frac{2\sin\phi'_{pt}}{\sqrt{3}\,(3+\sin\phi'_{pt})} \quad \text{at axisymmetric extension,} \tag{21}$$

$$\alpha_{pt}=\frac{\tan\phi'_{pt}}{\sqrt{9+12\tan^2\phi'_{pt}}} \quad \text{at plane strain condition,} \tag{22}$$

where ϕ'_{pt} is phase transformation angle and P_2 is defined in Fig. 7.

The Mohr-Coulomb yield surface shown in Eq. (13) is the most popular and practical in geomechanical field and the elliptical potential functions as shown in Eqs. (16) and (17) can obtain stable solutions because they have no corner. That is the reason that we employ the yield function and potential functions.

Supposing this is an isotropic hardening model with plastic volumetric strain ε_v^p as a hardening parameter, the yield stress I_c may be evaluated by means of the state surface concept (Kohgo et al., 1993a).

$$I_c=-3\exp\left(\frac{B^*-\varepsilon_v^p}{A^*}\right), \tag{23}$$

$$A^*=\frac{(\lambda^*-\kappa)}{2.3(1+e_0)}, \tag{24}$$

$$B^*=\frac{(\lambda_0^*-\kappa)}{2.3(1+e_0)}\ln(-p'_0)-\frac{(\Gamma_0^*-\Gamma^*)}{(1+e_0)}, \tag{25}$$

where κ is slope of e-log p' curves at unloading, e_0 is initial void ratio, p'_0 is initial mean effective stress and, λ_0^* and Γ_0^* are initial values of λ^* and Γ^*, respectively.

Subloading Surfaces

This model belongs to the original subloading surface model (Hashiguchi, 1980). Subloading surfaces are defined to be similar to the normal yield surfaces. The similar center is postulated to be consistent with the origin (*see* Fig. 8). The ratio of the sizes of subloading surfaces to the normal yield surfaces is defined as

$$\bar{R}=\frac{\bar{I}_c}{I_c} \quad (0\le\bar{R}\le 1), \tag{26}$$

where $\bar{I}_c$ is the value of I_c on the subloading surfaces. The value of $\bar{I}_c$ can be evaluated from the current stresses, because the current stress point is always lying on the subloading surfaces.

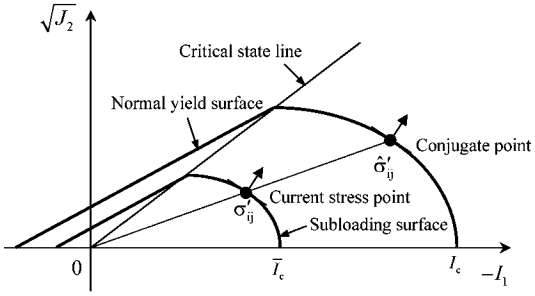

Fig. 8. Normal yield surfaces and subloading surfaces

A loading criterion is defined as follows.

$$\begin{aligned}&\dot{\bar{R}}>0 \quad \text{Loading,}\\ &\dot{\bar{R}}<0 \quad \text{Unloading,}\\ &\dot{\bar{R}}=0 \quad \text{Neutral loading,}\end{aligned} \tag{27}$$

where $\dot{\bar{R}}$ is increment of $\bar{R}$.

Let us consider a conjugate point on the normal yield surfaces with the same normal direction as the current effective stress point σ'_{ij} on the subloading surfaces. Then, the conjugate effective stress tensor $\hat{\sigma}'_{ij}$ is

$$\hat{\sigma}'_{ij}=\frac{\sigma'_{ij}}{\bar{R}}. \tag{28}$$

The hardening modulus H is postulated as

$$H=\hat{H}-\alpha_h\ln(\bar{R}), \tag{29}$$

where $\hat{H}$ is hardening modulus at conjugate point and α_h is a material parameter.

Procedure for estimation of stress and strain in elastoplastic range is as follows.

$$\dot{\sigma}'_{ij}=D^e_{ijkl}\dot{\varepsilon}^e_{kl}=D^e_{ijkl}[\dot{\varepsilon}_{kl}-\dot{\varepsilon}^p_{kl}], \tag{30}$$

$$\dot{\varepsilon}^p_{ij}=\dot{\lambda}\hat{n}^{\psi}_{ij}, \tag{31}$$

$$\dot{\lambda}=\frac{\hat{n}^f_{kl}D^e_{klmn}\dot{\varepsilon}_{mn}}{H+D^e_{abcd}\hat{n}^f_{ab}\hat{n}^{\psi}_{cd}}, \tag{32}$$

$$\hat{n}^f_{ij}=\frac{\dfrac{\partial f}{\partial\hat{\sigma}'_{ij}}}{\left[\left(\dfrac{\partial f}{\partial\hat{\sigma}'_{kl}}\right)\left(\dfrac{\partial f}{\partial\hat{\sigma}'_{kl}}\right)\right]^{1/2}}, \tag{33}$$

$$\hat{n}^{\psi}_{ij}=\frac{\dfrac{\partial \psi}{\partial\hat{\sigma}'_{ij}}}{\left[\left(\dfrac{\partial \psi}{\partial\hat{\sigma}'_{kl}}\right)\left(\dfrac{\partial \psi}{\partial\hat{\sigma}'_{kl}}\right)\right]^{1/2}}, \tag{34}$$

where $\dot{\sigma}'_{ij}$ is increment of effective stress tensor, D^e_{ijkl} is elastic modulus tensor, $\dot{\varepsilon}_{kl}$ is increment of strain tensor, $\dot{\varepsilon}^e$ is increment of elastic strain tensor, $\dot{\varepsilon}^p_{kl}$ is increment of plastic strain tensor, $\hat{n}^f_{ij}$ and $\hat{n}^{\psi}_{ij}$ are normal vectors to normal yield surfaces and plastic potential surfaces at conjugate point, respectively.

SIMULATIONS OF EXPERIENTAL TESTS

In order to verify the elastoplastic model, we conducted the simulations of the oedometer and triaxial compression tests of a rockfill named Material S (Kohgo et al., 2007). The K-G model was adopted to express the elastic properties.

$$K=\frac{-2.3(1+e_0)}{\kappa}+K_i, \tag{35}$$

$$G=G_i-\gamma_p p', \tag{36}$$

where K is bulk modulus, G shear modulus and K_i, G_i and γ_p material parameters.

Soil water retention properties were modeled by using Tangential model (Kohgo, 1997).

$$c = -\frac{\partial S_r}{\partial s} = -(1 - S_{re} + h_s S_{re}) \frac{P_a - s_e}{(P_a - s)^2} \quad (s \le s_e), \tag{37}$$

$$c = c_e + (c_m - c_e)\left(\frac{s - s_e}{s_m - s_e}\right)^{m_r} \quad (s_e < s \le s_m), \tag{38}$$

$$c = c_f + (c_m - c_f)\left(\frac{s - s_f}{s_m - s_f}\right)^{n_r} \quad (s_m < s \le s_f), \tag{39}$$

$$c = c_f \quad (s > s_f), \tag{40}$$

$$m_r = \frac{c_m(s_m - s_e) - (S_{re} - S_{rm})}{(S_{re} - S_{rm}) - c_e(s_m - s_e)}, \tag{41}$$

$$n_r = \frac{c_m(s_m - s_f) - (S_{rf} - S_{rm})}{(S_{rf} - S_{rm}) - c_f(s_m - s_f)}. \tag{42}$$

Where P_a is the atmospheric pressure, S_{re} is degree of saturation at air entry, h_s is Henry's coefficient of solubility ($=0.02$), and subscripts m and f denote respectively the values at the points F and M. Point F is the point with the lowest suction among the points where the tangential slope is almost constant and point M is the point where the tangential slope is the maximum (*see* APPENDIX).

The permeability was postulated to be a function of void ratio and degree of saturation as follows.

$$k = k_s \cdot E_p \cdot H_p, \tag{43}$$

$$E_p = \frac{1 + e_0}{1 + e}\left(\frac{e}{e_0}\right)^{n_p}, \tag{44}$$

$$H_p = \left(\frac{S_r - S_{rf}}{S_{re} - S_{rf}}\right)^{m_p}, \tag{45}$$

where k_s is the permeability at saturation, m_p and n_p are material parameters.

The simulations were conducted by using the saturated and unsaturated finite element consolidation analysis method (Kohgo, 1995, 1997; Kohgo et al., 2006). Quadratic iso-parametric elements for the displacement field and super-parametric elements for pore water pressure field were used.

Simulations of Oedometer Tests

Two series of oedometer tests (Kohgo et al., 2007): tests for the specimens with different initial degree of saturation S_{r0} and tests for the specimens soaked under constant vertical loads, were simulated. The finite element mesh and boundary conditions are shown in Fig. 9. The right half of the specimen was selected for the analyses. The boundary condition for displacement was set so that one dimension condition was satisfied. Seepage condition (suction is greater than or equal to 0) was satisfied on the upper surface of the specimen and undrained condition was postulated on the lower surface and both sides of the specimen. Inundated processes were simulated by reducing gradually suction values at all nodal points used to evaluate pore water pressures. This procedure was adopted to save calculation times and obtain stable solutions. The parameters used in the simulations are shown in Table 2. The procedures for determination of parameters concerned with unsaturated properties are shown in the APPENDIX.

Simulation results are shown in Figs. 10, 11 and 12. Figure 10 shows e-log σ_v (total vertical stress) relation-

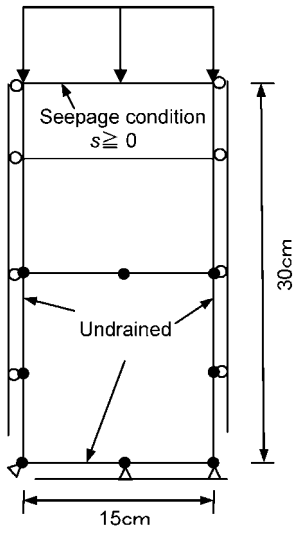

Fig. 9. Finite element mesh and boundary conditions for simulations of oedometer tests

Table 2. Material parameters used in simulations

Elasticity			Subloading Plasticity					
κ	K_i (kPa)	G_i (kPa)	γ_p	α_h (kPa)	ϕ'	ϕ'_{cs}	ϕ'_{pt}	R
0.005	3,500	5,300	100	1×10^4	42.3°	42.5°	42.5°	1.0
State surface								
λ	Γ	e^0_{01}	a^*_1 (kPa)	λ^*_{f1}	s^*_m	e^{02}_0	a^*_2 (kPa)	λ^*_{f2}
0.158	0.872	0.00	0.403	0.093	1.006	1.535	5.75	0.02
Soil water retention								
S_{re}	S_{rm}	S_{rf}	s_e (kPa)	s_m (kPa)	s_f (kPa)	c_m (kPa^{-1})	c_f (kPa^{-1})	
0.85	0.50	0.20	0.07	0.50	5.00	1.0×10^0	4.0×10^{-3}	
Permeability								
k_s (m/min)	m_p	n_p						
1×10^2	3	3						

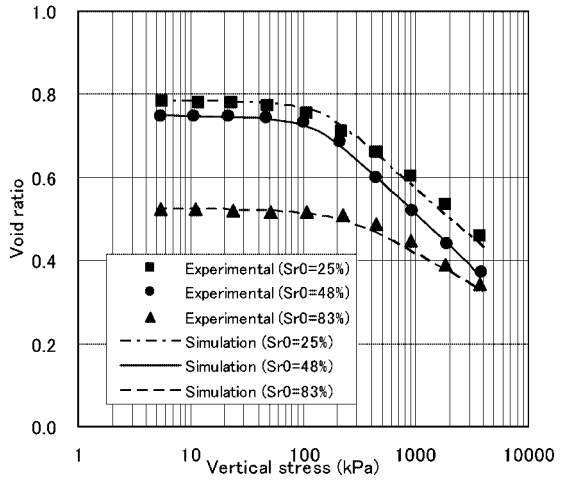

Fig. 10. Simulation results of the oedometer tests without soaking for a rockfill named Material S

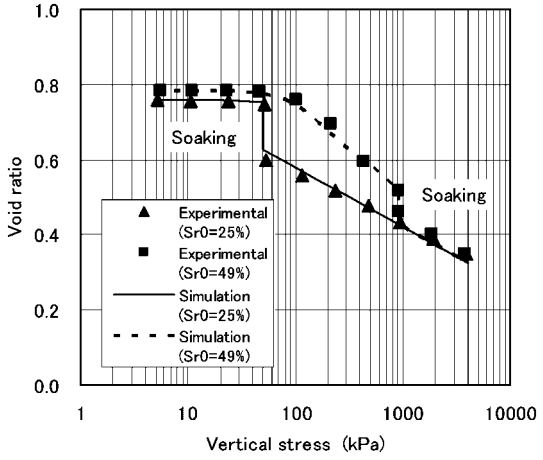

Fig. 11. Simulation results of the oedometer tests with soaking for a rockfill named Material S

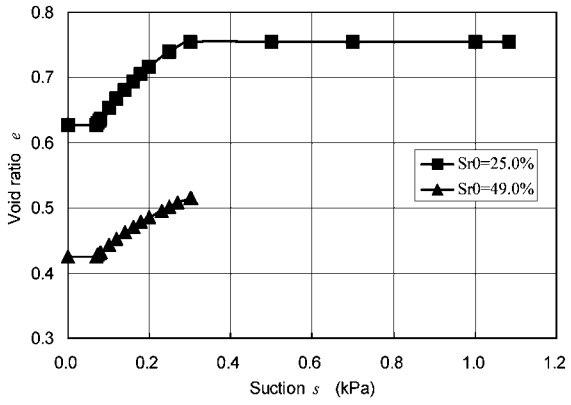

Fig. 12. The calculated relationships between suction and void ratio during soaking

ships of specimens without soaking. The symbols shown in the figure denote the experimental results and the solid and dashed lines denote the simulation results. The following experimental evidences were obvious from Fig. 10. The slopes of e-log σ_v curves in the normally consolidation region depend on the initial degree of saturation of the specimens. The slope of the specimen with initial degree of saturation $S_{r0}=48\%$ is the maximum among three specimens and that of the specimen with $S_{r0}=83\%$ is the minimum. In overconsolidation region, the slopes of e-log σ_v curves are almost constant without influence of the initial degree of saturation. These experimental properties described above could be well expressed by the analyses.

Figure 11 shows e-log σ_v relationships of specimens with soaking. The great amount of volume reductions due to wetting could be seen in both experiment and simulation results. The stress paths after soaking trace on a unique line that is consistent with the e-log σ_v line of the specimen with $S_{r0}=83\%$. In this rockfill, the amount of volume reduction due to wetting decreases as the vertical stress increases. The simulation results well agreed with the experimental ones. The calculated relationships between suction and void ratio during soaking are shown in Fig. 12. As the specimen with $S_{r0}=25\%$ was under overconsolidation region, little volume reduction occurred until suction reached about 0.3 kPa. After $s=0.3$ kPa the remarkable volume reductions were induced by wetting. Meanwhile the specimen with $S_{r0}=49\%$ had remarkable volume reduction from the commencement of wetting. Because the specimen lay on the normal consolidation surface (state surface) before wetting. Thus once stress paths encountered the state surface, remarkable volume reduction occurred.

Simulations of Triaxial Compression Tests

The three series of tests (Kohgo et al., 2007): tests for the saturated specimens, tests for the unsaturated specimens and tests for the specimens soaked during shearing, were simulated. The finite element mesh and boundary conditions are shown in Fig. 13. The right and upper quarter of the specimens was selected for the analyses. Axial symmetric problems were set. For unsaturated specimens, seepage condition was satisfied on the upper surfaces of the specimens and undrained condition was postulated on the bottom and both sides of the specimens. Inundated processes were simulated by the same procedure used in the simulations of oedometer tests. The shearing process was simulated by applying constant vertical displacements per time to the nodal points on the upper surface of the specimens. The parameters used in the simulations are also shown in Table 2.

Simulation results are shown in Figs. 14, 15, 16 and 17. Figure 14 shows the simulation results of saturated specimens. The thick and thin lines denote the simulation and experimental results, respectively. The stress-strain relationships calculated were well consistent with the experimental ones. However, the volumetric strain vs. axial strain relationships calculated were a little bit departed from the experimental ones and the calculated relationships were almost expressed as a curve.

Figure 15 shows the simulation results of unsaturated specimens. Though both experimental and simulation

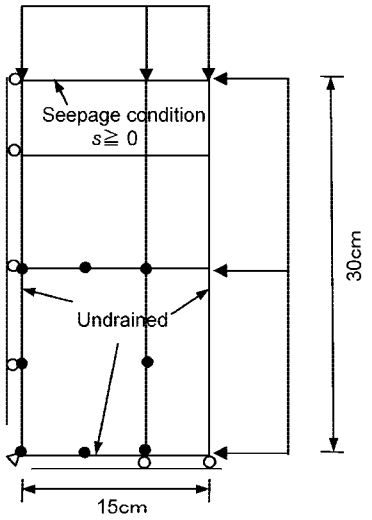

Fig. 13. Finite element mesh and boundary conditions for simulations of triaxial compression tests

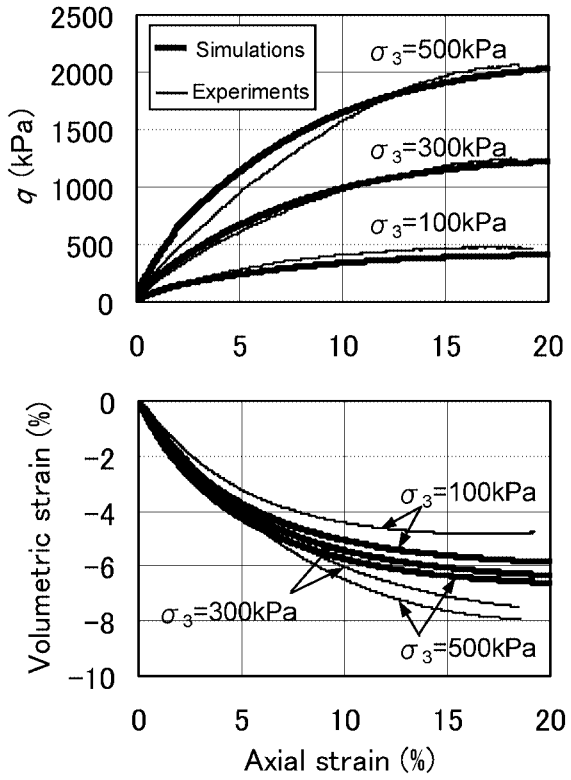

Fig. 14. Simulation results of the triaxial compression tests for saturated specimens of a rockfill named Material S

results expressed strain-softening behavior in low confining stress, the level of strain softening decreased as the confining stresses increased. Especially, the stress-strain relationship of the specimen with $\sigma_3 = 100$ kPa was consistent with the experimental one. The simulation results well expressed that shear strength magnitudes of unsaturated specimens were greater than those of saturated ones. The estimated stress-strain relationship well agreed with the experimental ones.

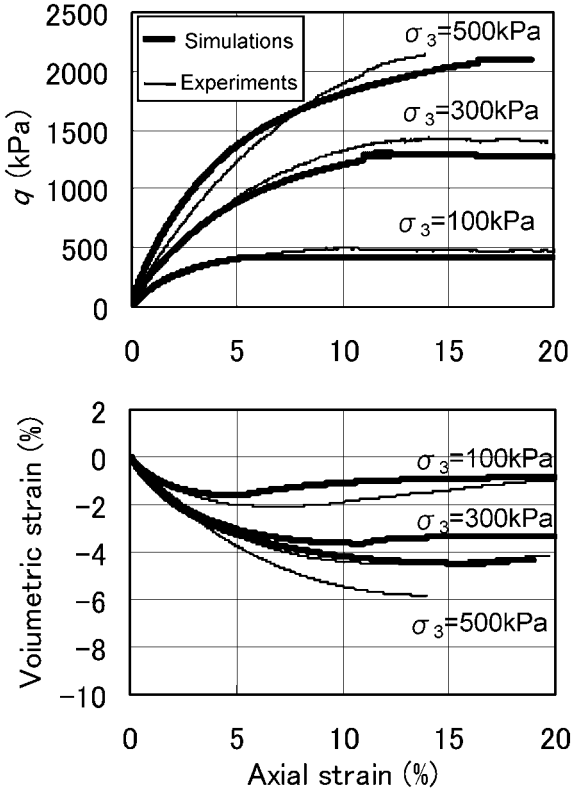

Fig. 15. Simulation results of the triaxial compression tests for unsaturated rockfill specimens of a rockfill named Material S

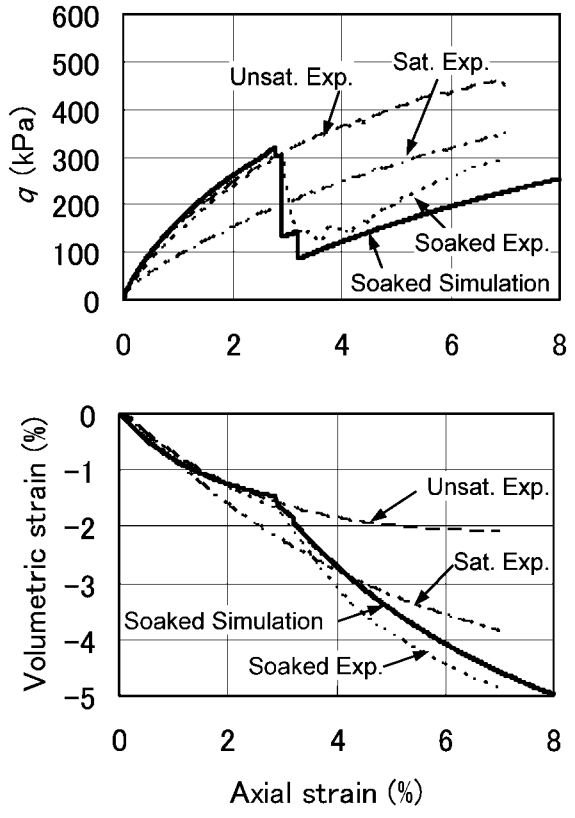

Fig. 16. Simulation result of the triaxial compression test for the specimen with $\sigma_3 = 100$ kPa soaked during shearing of a rockfill named Material S

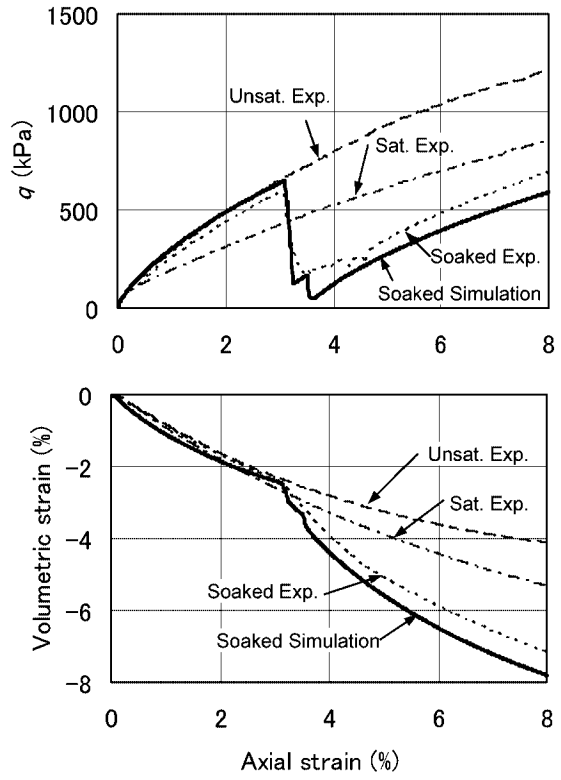

Fig. 17. Simulation result of the triaxial compression test for the specimens with $\sigma_3 = 300$ kPa soaked during shearing of a rockfill named Material S

Figures 16 and 17 show the simulation results of the specimens soaked during shearing. Figures 16 and 17 are the results of the specimens with $\sigma_3 = 100$ kPa and $\sigma_3 = 300$ kPa, respectively. The simulated results could well express the behavior that deviator stresses during soaking decreased and were smaller than those of the saturated specimen. The remarkable volume reduction during inundation occurred in both experimental and simulation results and the axial strain-volumetric strain relationships stayed below those of the saturated specimens. The reason that the q-ε_a and ε_a-ε_v relationships after inundation are not consistent with those of the saturated specimens is as follows. The amounts of volume reductions due to consolidation pressures in the saturated specimens are greater than those in the soaked specimens, because the soaked specimens were under the air dry condition during the consolidation. The different volume reductions between saturated and soaked specimens during the consolidation may be induced during the inundation. Then the q-ε_a and ε_a-ε_v relationships of soaked specimens after inundation were not consistent with those of the saturated specimens.

Thus, we could well simulate not only consolidation behavior but also shear one by using this elastoplastic model.

CONCLUSIONS

We proposed an elastoplastic model for unsaturated rockfills that was applicable for both compression and shear. The model was constructed by a simple modification of the generalized elastoplastic model for unsaturated soils proposed by authors(1993b). To verify the elastoplastic model, the simulations of the oedometer and triaxial compression tests for a rockfill were carried out. The simulation results could well express both saturated and unsaturated mechanical behavior of the rockfill.

NOTATION

a_1^*, a_2^* material parameters for state surface
e void ratio
e_0 initial void ratio
e_{01}^0, e_{02}^0 material parameters for state surface
f critical state line
f_1 normal yield surface (failure surface)
f_2 normal yield surface (cap surface)
$\hat{n}^f$ normal vectors to normal yield surface at conjugate point
$\hat{n}_{ij}^{\psi}$ normal vectors to plastic potential surface at conjugate point
D_{ijkl}^e elastic modulus tensor
G shear modulus.
H hardening modulus
$\hat{H}$ hardening modulus at conjugate points
I_1 the first stress invariant
I_c yield stress
$\bar{I}_c$ value of I_c on subloading surfaces
J_2 the second invariant of deviator stress
K bulk modulus
K_i, G_i, γ_p material parameters for elastic modulus.
p' mean effective stress
q deviator stress
p'_0 initial mean effective stress
R material parameter for aspect ratio of elliptical cap yield surface
$\bar{R}$ size ratio of subloading surfaces to normal yield surfaces
$\dot{\bar{R}}$ an increment of $\bar{R}$
s suction
s^* effective suction
s_e air entry suction
S_{r0} initial degree of saturation
u_a pore air pressure
u_{ae} pore air pressure at air entry
u_w pore water pressure
α_h material parameter for hardening modulus of subloading surfaces
Γ value of Γ^* at saturation
Γ^* void ratio of e-log p' curves at $p' =$ unit
Γ_0^* initial values of Γ^*
$\dot{\varepsilon}_{kl}$ increment of strain tensor,
$\dot{\varepsilon}_{kl}^p$ increment of plastic strain tensor
ε_v^p plastic volumetric strain
θ Lode angle
κ slope of e-log p' curves at unloading
λ value of λ^* at saturation
λ^* slope of e-log p' curves

λ_0^* initial values of λ^*
λ_{f1}^*, λ_{f2}^* material parameters for state surface
σ total stress
σ' effective stress
σ'_1, σ'_2, σ'_3 effective principal stresses
σ'_{ij} effective stress tensor
$\dot{\sigma}'_{ij}$ increment of effective stress tensor
$\hat{\sigma}'_{ij}$ conjugate effective stress tensor
σ'_v vertical effective stress
ϕ' internal friction angle of failure line
ϕ'_{cs} internal friction angle of critical state line
ϕ'_{pt} internal friction angle of phase transformation line
ψ_1, ψ_2 elliptical plastic potential functions

REFERENCES

1) Fleureau, J. M., Kheirbek-Saoud, S., Soemitro, R. and Taibi, S. (1993): Behavior of clayey soils on drying-wetting paths, *Can. Geotech. J.*, **30**, 287–296.
2) Gan, J. K. M., Fredlund, D. G. and Rahardjo, H. (1988): Determination of the shear strength parameters of an unsaturated soil using the direct shear test, *Can. Geotech. J.*, **25**, 500–510.
3) Hashiguchi, K. (1980): Constitutive equations of elastoplastic materials with elastic-plastic transition, *J. Appl. Mach.*, ASME, **47**, 266–272.
4) Kohgo, Y. (1987): The interpretations and analyses of mechanical behavior of partly saturated soils using elastoplastic models, *Proc. Sym. Unsaturated Soils*, Osaka, JGS, 69–78 (in Japanese).
5) Kohgo, Y., Nakano, M. and Miyazaki, T. (1993a): Theoretical aspects of constitutive modeling for unsaturated soils, *Soils and Foundations*, **33**(4), 49–63.
6) Kohgo, Y., Nakano, M. and Miyazaki, T. (1993b): Verification of the generalized elastoplastic model for unsaturated soils, *Soils and Foundations*, **33**(4), 64–73.
7) Kohgo, Y. (1995): A consolidation analysis method for unsaturated soils coupled with an elastoplastic model, *Proc. 1st Int. Conf. Unsaturated Soils*, Paris, 1085–1093.
8) Kohgo, Y. (1997): Method of analysis of saturation collapse behavior, *Japan International Research Center for Agricultural Sciences*, **4**, 1–28.
9) Kohgo, Y., Asano, I. and Tagashira, H. (2001): Modelling of state surfaces of unsaturated soils, *Proc. Int. Sym. Suction, Swelling, Permeability and Structure of Clay, Clay Science for Engineering (IS-Shizuoka)*, Shizuoka, 467–474.
10) Kohgo, Y., Takahashi, A., Asano, I. and Suzuki, T. (2006): FEM consolidation analysis of centrifuge test for rockfill dam model during first reservoir filling, *Geotechnical Special Publication*, ASCE, **147**, 2312–2323.
11) Kohgo, Y., Asano, I. and Hayashida, Y. (2007): Mechanical properties of unsaturated low quality rockfills, *Soils and Foundations*, **47**(5), 947–959.
12) Marachi, N. D., Chan C. K., Seed, H. B. and Duncan, J. M. (1968): Strength and deformation characteristics of rockfill materials, Dept. of Civil Eng., *Report No. TE-69-5*, University of California, Berkeley.
13) Marsal, R. J. (1972): Mechanical properties of rockfill, *Casagrande Volume*, John Wiley & Sons, 109–200.
14) Nobari, E. S. and Duncan, J. M. (1972): Effect of reservoir filling on stresses and movements in earth and rockfill dams, Dept. of Civil Eng., *Report No. TE-72-1*, University of California, Berkeley.
15) Oldecop, L. A. and Alonso, E. E. (2001): A model for rockfill compressibility, *Geotechnique*, **51**(2), 127–139.
16) Terzaghi, K. (1960): Discussion on settlement of Salt Springs and Lower Bear River concrete face dams, *Trans. ASCE*, **125**(2), 139–148.
17) Zienkiewicz, O. C. and Humpheson, C. (1977): Viscoplasticity: A generalized model for description of soil behaviour, *Numer. Meth. Geotech. Eng.*, edited by Desai, C. S. and Christian, J. T., New York, McGraw-Hill, 116–147.

APPENDIX: DETERMINATION OF PARAMETERS FOR SOIL WATER RETENTION CURVE AND STATE SURFACE

Tangential Model for Soil Water Retention Curve

In Tangential model, three points are selected to predict a soil water retention curve obtained from soil water retention tests (*see* Fig. A–1). The three points are denoted as F, M and E. The point F is the point with the lowest suction among the points where the tangential slope is almost constant, the point M is the point where the tangential slope is maximum and the point E is the air entry point. The values of degree of saturation S_r, suction s and tangential slope of soil water retention curve $c(=-\partial S_r/\partial s)$ are identified from the soil water retention curve obtained. It is very difficult to identify the point E for rockfill materials. Here we supposed that $S_{re}=0.85$ and $s_e=0.07$ kPa (nearly equal to 0.0) because the e-log σ_v relationship obtained from oedometer tests shows that the relationship is almost consistent with the ones of specimens soaked when $S_r \geq 0.85$.

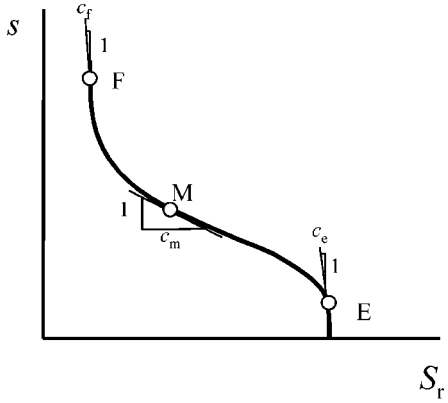

Fig. A–1. A typical soil water retention curve and three input points for Tangential model

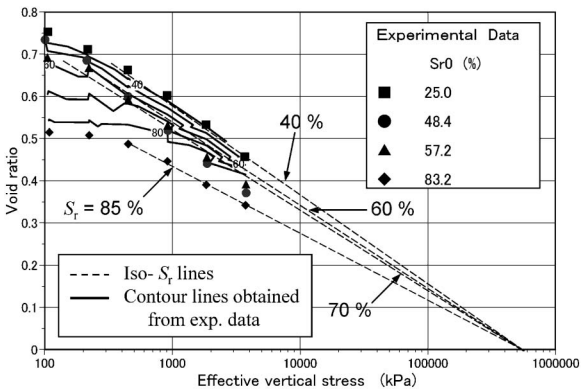

Fig. A–2. Iso-degree of saturation lines estimated from oedometer test data

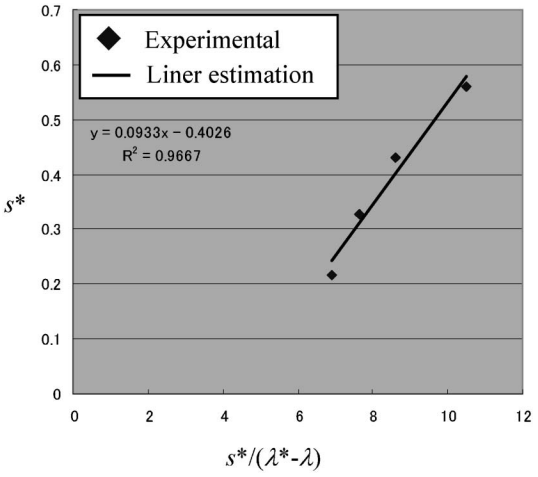

Fig. A–3. A linear relationship between s^* and $s^*/(\lambda^*\text{-}\lambda)$

State Surface

We adopted the following procedure to identify parameters for state surface: 1) determine λ and Γ by using e-log p' relationship obtained from the oedometer test data for almost saturated and soaked specimens. Here mean effective stresses are calculated by $p' = (1 + 2K_0)\sigma'_v/3$ and K_0 value is estimated by using Jaky's equation $1 - \sin\phi'$, 2) draw iso-degree of saturation ε-log σ'_v lines as shown in Fig. A–2 from oedometer test results, 3) these lines intersect at a point. The value of void ratio at the intersect point is e^0_{01}, 4) read the slopes λ^* of the isolines, 5) draw a graph shown in Fig. A–3, 6) from Eq. (8), the following linear relationship is valid: $s^* = \lambda^*_{f1}[s^*/(\lambda^* - \lambda)] - a^*_1$, so you can estimate parameters λ^*_{f1} and a^*_1 from Fig. A–3, and 7) if you have more data, you may identify parameters λ^*_{f2} and a^*_2 by using the same operations 2) to 6). Here, the e-log σ'_v line had the maximum slope at $S_r = 25\%$, so $s^*_m = 1.006$ kPa was identified by using the Tangential model.